Metallurgical modeling of microcrack repairment during welding nonferrous materials: non-equilibrium solidification behavior of weld pool (I)

Gao Zhiguo
高志国 *

Abstract *Metallurgical modeling of synergistic microcrack self-repairmen during welding single crystal and polycrystalline superalloys of high-temperature aerospace materials has been properly established. The idea of improvement of nickel-based superalloys weldability through non-equilibrium solidification behavior of backfill to self-repair arterial crack network is usefully proposed. Crystallographic control strategy of crack self-repairmen of fusion zone interdendritic solidification cracking and heat-affected zone (HAZ) intergranular liquation cracking is technically achievable, indicating that optimal niobium alloying beneficially refines weld microstructure, stabilizes the primary solidification path, increases the solidification temperature and concomitantly decreases the weld pool geometry. High-carbon grain boundary is more thermal stable and less contributes to incipient intergranular liquid film than that of low-carbon grain boundary. The theoretical predictions of cracking susceptibility are indirectly verified in a rather satisfactory manner. Additionally, the metallurgical modeling enhances predicative capabilities and thereby is readily applicable for other alloy systems.*

Key words metallurgical modeling, nickel alloys, solidification behavior, cracking repairmen

doi: 10.3969/j.issn.1004-5341.2017.02.005

0 Introduction

Normally, the availability of single crystal or polycrystalline superalloys is particularly limited either by interdendritic solidification cracking of fusion zone or intergranular liquation cracking of HAZ. Despite of the considerable difference in chemistry, complete or partial healing of interior crack in fusion zone and HAZ by backfill is considered to be the primary reason for the improvement of weld ability of newly developed nickel-based superalloys. Vitek et al.[1] theoretically analyzed the effect of welding conditions on stray grain formation in single crystal welds. Dye et al.[2] developed the general model to predict centerline grain boundary, interdendritic microporosity, constitutional liquation and solidification cracking during the tungsten-inert gas (TIG) welding of nickel alloys. Liu et al.[3] introduced a mathematical modeling to study the effect of geometrical parameters of weld pool on crystal growth and microstructure development during laser surface melting of single crystal alloys. Trivedi and Kurz et al.[4-5] extended the linear perturbation theory and eutectic growth model under rapid solidification conditions. Wang et al.[6] introduced dendrite growth model for rapid solidification of multi-component alloys to describe the evolution of interface. Galenko et al.[7] used sharp-interface modeling and phase-field simulation to predict the dendritic rapid solidification. These previous theoretical models are valid by the experiments, but did not couple each other. No systematic model has been proposed to describe contributing factors to microcrack repairmen under non-equilibrium solidification behavior of weld pool. The

Received date: 2016-11-09

* Gao Zhiguo, Aerospace Research Institute of Materials and Processing Technology, Beijing, 100076. Gao Zhiguo, Corresponding author, E-mail: gaozhiguo_anthony@163.com

objective of this work arises from the scarcity of pertinent mathematical modeling on amelioration of cracking and the existing methods are incorporated into one model to further predict the cracking susceptibility and self-repairmen in more quantitative senses.

1 Mathematical model

In order to establish reasonable mathematical modeling, several necessary assumptions are made in this work unless otherwise stated: (I) heat transfer equation is solved by the heat dissipation through conduction within the material of constant properties; (II) dendrite tip grows marginally with the absolute stability of planar interface at high velocity under constrained growth conditions; (III) the solubility limit extension is neglected and the matrix composition is uniform on a microscopic scale; (IV) dissolution of niobium carbide particle in the subsolidus part of HAZ will commence just above the dissolution temperature and continue until niobium carbide reprecipitates during solidification; (V) liquid diffusion coefficient of niobium in the molten weld pool increases due to local overheating.

1.1 Non-equilibrium solidification behavior of weld pool

1.1.1 Dendrite growth velocity and temperature gradient

Rosenthal thick plate solution characterizes the three-dimensional temperature distribution at pseudo-steady state as follows:

$$T - T_{\circ} = \frac{q\eta}{2\pi\lambda}\left(\frac{1}{R}\right)\exp\left[-\frac{v}{2a}(R + x)\right] \tag{1}$$

where $R = \sqrt{x^2 + y^2 + z^2}$, $T_{\circ}$ is the ambient temperature; λ is the thermal conductivity; q is the welding power; η is efficiency factor owing to heat losses by convection and radiation; v is the welding speed in x direction; a is the thermal diffusivity.

θ is the angle between the surface normal of solidification boundary $\boldsymbol{n}$ and the velocity v_{100} on the top surface of weld pool; φ is the angle between the surface normal of solidification interface $\boldsymbol{n}$ and v_{010} in the transverse cross-section. In the x-y plane, where $\varphi = 0$ and $0 \leqslant \theta \leqslant 180°$, the solidification interface velocity v_{s} is given by:

$$v_{\mathrm{s}} = v\cos\theta = v\frac{G_x}{|\boldsymbol{G}|} \tag{2}$$

In the $y - z$ plane, where $\theta \approx 90°$, $\cos\varphi$ is calculated by the following:

$$\cos\varphi = \frac{G_y}{|\boldsymbol{G}|} \tag{3}$$

where G_x, G_y, G_z are the temperature gradient components, and $|\boldsymbol{G}| = \sqrt{G_x + G_y + G_z}$.

The local dendrite growth velocity and temperature gradient are given, respectively:

$$v_{\mathrm{d}} = \frac{v_{\mathrm{s}}}{\cos\psi} = \frac{v\cos\theta}{\cos\psi} \tag{4}$$

$$G_{\mathrm{d}} = |\boldsymbol{G}|\cos\psi \tag{5}$$

$$\cos\psi = u_x\cos\theta + \sin\theta(u_y\cos\varphi + u_z\sin\varphi) \tag{6}$$

where ψ is the misalignment angle between the solidification front normal and arbitrary dendrite growth direction; $\boldsymbol{u}_{\mathrm{hk}}$ is the unit vector along [hkl] dendrite growth direction.

1.1.2 Stability of the advancing solidification front

The non-equilibrium nature of welding determines the solidification behavior, and growth kinetics of dendrite tip is given by KGT model[8]:

$$\frac{4\pi^2\Gamma}{r_{\mathrm{d}}^2} + \frac{2PmC_{\circ}(1 - k)\xi_{\mathrm{c}}}{[1 - (1 - k)Iv(P)]r_{\mathrm{d}}} + G = 0 \tag{7}$$

where $C_{\circ}$ is the initial liquid concentration; $Iv(P)$ is Ivantsov's solution; Γ is the Gibbs-Thomson coefficient; m is the liquidus slope; G is the mean temperature gradient at the interface; k is the partition coefficient; P is the solutal Peclet number; r_{d} is the dendrite tip radius.

$$\xi_c = 1 - \frac{2k}{\sqrt{1 + \left(\frac{2\pi}{P}\right)^2} - 1 + 2k} \tag{8}$$

Partition coefficient is dependent on interface velocity and temperature as follows:

$$k = \frac{k_\circ + \left(\frac{a_\circ v_s}{D_L}\right)}{1 + \left(\frac{a_\circ v_s}{D_L}\right)} \tag{9}$$

where $k_\circ$ is the equilibrium partition coefficient; $a_\circ$ is related to the interatomic distance; D_L is the diffusivity in liquid.

1.1.3 Solidification microstructure development

The dendrite trunk spacing in the vicinity of mushy zone is given by:

$$\lambda_1 = \left(\frac{3\Delta T^* r_d}{G}\right)^{\frac{1}{2}} \tag{10}$$

where ΔT^* is difference between tip temperature and non-equilibrium solidus.

The development of secondary dendrite arm spacing during weld pool solidification is given by:

$$\lambda_2 = 5.5(Mt_\circ)^{\frac{1}{2}} \tag{11}$$

where $t_\circ$ is the local solidification time and M is a mobility term in regards to the phase diagram, respectively.

$$t_\circ = \frac{g}{v_s} = \frac{\Delta T^*}{Gv_s} \tag{12}$$

$$M \approx \frac{\Gamma D_L \ln\left(\frac{C_E}{C_\circ}\right)}{m_E(1-k)(C_\circ - C_E)} \tag{13}$$

where C_E is the eutectic concentration and m_E is the slope of liquidus curve under the non-equilibrium solidification conditions.

1.1.4 Solute redistribution at dendrite tip

For Ivantsov's solution around parabolic interface,

$$\Omega = \frac{C_l^* - C_\circ}{C_l^* - C_s} = \frac{C_l^* - C_\circ}{C_l^*(1-k)} = Iv(P) \tag{14}$$

where Ω is supersaturation, C_l^* is the liquid composition at the dendrite tip, C_s is the solid concentration at the interface.

The tip temperature T_t is given by:

$$T_t = T(C_l^*) - \Delta T \tag{15}$$

where $T(C_l^*)$ is the liquid temperature corresponding to the concentration C_l^*, ΔT is the minimum undercooling.

After introducing some relationships in the SA model[9], the amount of eutectic-type constitute, f_E, is rewritten by:

$$f_E = (1-\Omega)\left(\frac{\frac{C_s^{\max}}{kC_l^*} - \frac{\alpha_E}{k-1}}{1 - \frac{\alpha_E k}{k-1}}\right)^{\frac{1}{k-1}} \tag{16}$$

where $\alpha_E = \frac{D_L}{m_E} v_s C_\circ$.

1.2 Dissolution of niobium carbide particle in the subsolidus part of HAZ

The general case of particle dissolution is given by:

$$\frac{f}{f_\circ} = \left(1 - \frac{2}{r_\circ^2}\int_{t_1}^{t_2} \frac{C_i - C_m}{C_p - C_i} D_L \mathrm{d}t\right)^{\frac{3}{2}} \tag{17}$$

where C_m is the concentration in matrix; t_1 and t_2 are the total time spent on dissolution of niobium carbide particle; $f_\circ$ is the initial particle volume fraction; $r_\circ$ is the initial particle radius.

The concentration of niobium at the NbC-matrix interface, C_i is obtained via the solubility product as follows:

$$C_i = \frac{\exp\left(\frac{\Delta S^\circ}{R}\right)}{C_c}\exp\left(\frac{-\Delta H^\circ}{RT}\right) \quad (18)$$

where R is the universal gas constant; C_c is the carbon concentration; ΔS° is the standard entropy of reaction; ΔH° is the standard enthalpy of reaction.

The concentration of niobium in the NbC is given by:

$$C_p = \frac{M_{Nb}}{M_{Nb} + M_c} \quad (19)$$

where M_{Nb} and M_c are the atomic weights of niobium and carbon, respectively.

1.3 HAZ grain grow in the present of dissolving particle

HAZ grain either immediately coarsens until it is thermodynamically stable up to a limiting grain size by unpinning of grain boundaries or is refined because of the occurrence of substantial liquid film migration. The resulting average grain size in the presence of dissolving particle is given by:

$$\overline{D} = \frac{(\overline{D}_\circ)^2}{(\overline{D}_\circ)^2 - \left(\frac{k_z}{f_\circ}\right)^2\left(2\int_{t_1}^{t_2}\alpha D_L \mathrm{d}t\right)} \quad (20)$$

where k_z is the zener coefficient, α is the dimensionless supersaturation.

1.4 Evolution of intergranular liquid film in the subsolidus part of HAZ

With assumption that the NbC-matrix interface is flat and metastable liquid continuously distributes along the grain boundaries, RT model[10] correlated the volume fraction of niobium carbide and the grain size with the cumulative thickness of intergranular liquid film as follows:

$$L = \frac{\left(\frac{\overline{D}}{2}\right)\left(\frac{f_{NbC}}{\rho_{NbC}}\right)}{\frac{f_{NbC}}{\rho_{NbC}} + \frac{f_\gamma}{\rho_\gamma}} \quad (21)$$

where ρ_{NbC} and ρ_γ are the densities of NbC and γ, f_{NbC} and f_γ are the weight fractions of NbC and γ.

1.5 Sensitive time interval of cracking

The characteristic time duration from onset of niobium carbide particle dissolution to liquidus temperature of the molten weld pool and then down to actual solidus temperature is defined as a criterion to assess the material resistance or susceptibility to cracking as follows:

$$\Delta t_s = t_E - t_D \quad (22)$$

where t_E is the time of depressed eutectic temperature during non-equilibrium solidification; t_D is the time of incipient dissolution of niobium carbide particle during on-heating part of weld thermal cycle.

2 Experiments

Wrought 718-type derivative nickel-based superalloy is used and the chemical composition suffices the following upper limit, 54.4Ni – 17.9Cr – 17.6Fe – 5.4Nb – 2.9Mo – 0.9Ti – 0.5Al – 0.05Si – 0.05Mn – 0.04B – 0.026C – 0.007P – 0.0014Mg (wt.%). The samples of dimension 80 mm × 15 mm × 6 mm were subjected to 1 050 ℃ pre-weld solution heat treatment for one hour and followed by air cooling for bead-on-plate laser welding. Subsequently, weld sections were prepared by metallographic technique. Total crack length was morphologically measured by optical microscopy and scanning electron microscopy (SEM) in ten sections of each weld. The relevant data applicable to the calculation from miscellaneous sources are listed in Table 1.

3 Results and discussion

3.1 Effect of welding parameters on the weld pool geometry

The dependence of the fusion boundary on the welding parameters is shown in Fig. 1. In Fig. 1a, the scale of penetration rapidly shrinks and becomes narrow when abatement of heat input, that is, less laser power or high welding speed. The calculated range of the depth is lower than that of experimental one thanks to uncertainty of the absorptivity of laser beam with process instability to loss

the transferable energy. In Fig. 1b, initially, the elliptical temperature profiles are expanded behind the laser beam and widely compressed ahead of the molten weld pool owing to the relative advance of the solid-liquid interface during increment of laser power. The predicted range of weld pool maximum width is 1.193 to 2.363 mm, which is reasonably close to the range of experimental results of 1.122 to 2.428 mm.

Table 1 List of thermophysical properties and relevant data for the calculation

Properties	Connotation	Unite	Value	Reference
a	Thermal diffusivity	mm^2/s	3.38	[11]
$\alpha_\circ$	Length scale	nm	5.00	[8]
λ	Thermal conductivity	W/mm℃	0.017 60	[11]
ρc	Volume heat capacity	J/mm^3℃	0.003 56	[11]
Γ_{NbC}	Gibbs-Thomson coefficient	mm℃	0.000 095 8	[9,12]
Γ_{Laves}	Gibbs-Thomson coefficient	mm℃	0.000 20	[9,13]
D_L	Diffusion of niobium	mm^2/s	$1.04\exp(-202\ 590/RT)$	[14]
m_{NbC}	Slope of the liquidus curve	℃ per wt%	−11	[10]
m_{Laves}	Slope of the liquidus curve	℃ per wt%	−11.85	[15]
ρ_{NbC}	Density of niobium carbide	kg/m^3	6 500	[16]
$\Delta S°$	Standard entropy of reaction	JK/mol	43.26	[16]
$\Delta H°$	Standard enthalpy of reaction	J/mol	129 578	[16]
C_s^{Max}	Maximum solid solubility	wt%	9.30	[15]
$M_\circ^*$	Modified kinetic constant	$\mu m^2/s$	37×10^9	[16]
$k_\circ$	Equilibrium partition coefficient		0.47	[15]
$\overline{D}_\circ$	Initial grain size	μm	98.8	
η	Efficiency factor		0.36	

3.2 Effect of crystallographic orientation and niobium alloying on the microstructural morphology of single crystal superalloys

The surface, (001) and (0311), and laser beam directions, [100] and [110], are considered. The effect of processing configurations on the scale of dendrite trunk spacing and dendrite transition regime under constrained growth conditions is showed in Fig. 2. In Fig. 2a, the dendrite trunk spacing initially reduces and then increases for (001) ∥ [110] when only half of the top surface of weld pool taking into account. On the left side of the weld pool, [$0\bar{1}0$] and [100] dendrites grow preferentially, whereas on the right side, [010] and [100] dendrites are dominant for the (001) ∥ [100] and (0311) ∥ [100]. The significant shifts in the transitional boundary between the [010], [100] and [$0\ \bar{1}0$] locate at $\theta = 45°$ and 135° for the (001) ∥ [100], and 46° and 134° for the (0311) ∥ [100], respectively. In Fig. 2b, only the right side of the transverse cross-section of the weld pool is especially considered. The dendrite trunk spacing initially increases and then decreases after exceeding the intersection of dendrite boundaries along the solid-liquid interface; the dendrite trunk spacing of (0311) ∥ [100] is of particular interest since it is almost the smallest. There are only [010] and [001] dendrites growth, and the obvious transition boundaries are locally characterized by $\varphi = 45°$, 35.3°

and 60.3° for the (001)||[100], (001)||[110] and (0311)||[100], respectively.

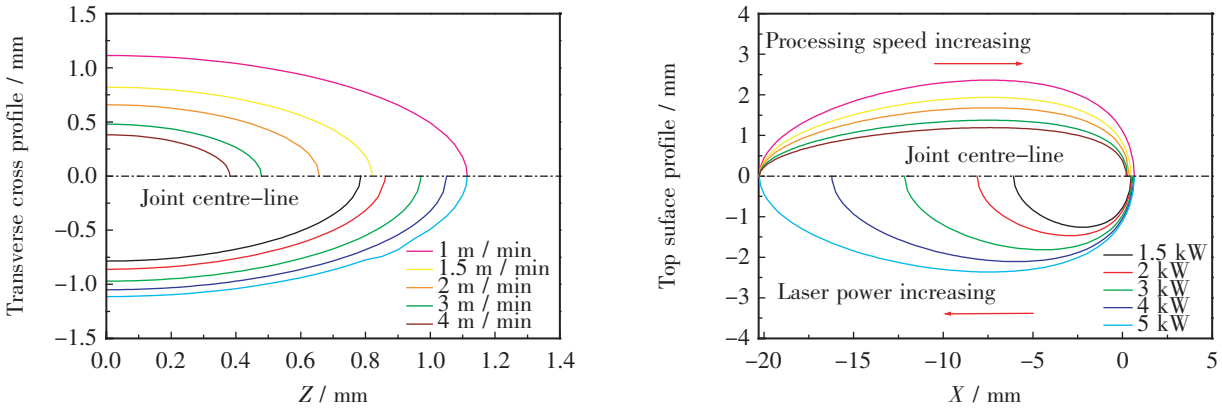

(a) Transverse cross-section (b) Top surface

Fig. 1 The role of welding parameters in weld pool profiles

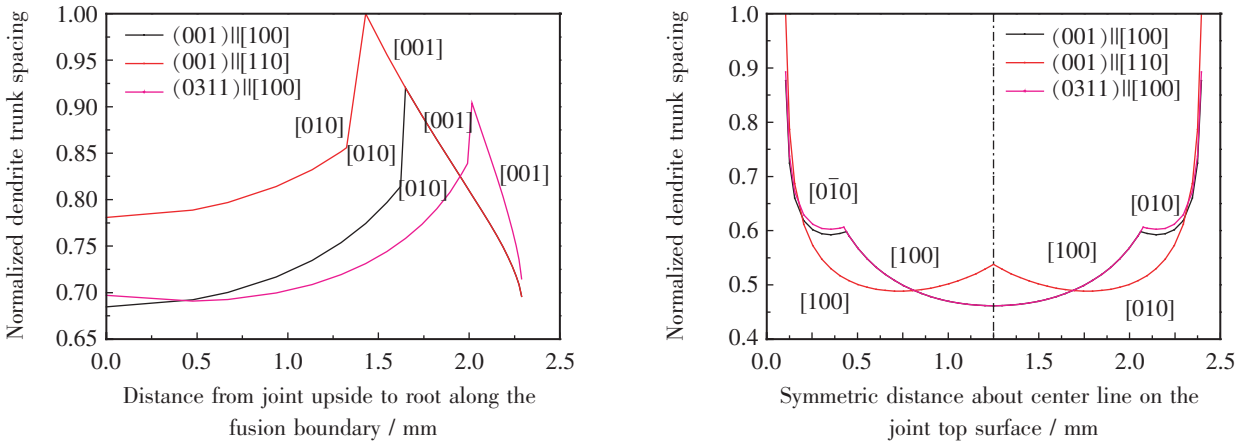

(a) Longitudinal dendrite morphology (b) Transverse dendrite morphology

Fig. 2 The role of crystallographic orientation in dendrite morphology

The scale of dendrite trunk spacing is strongly dependent on the shape of weld pool and niobium alloying as shown in Fig. 3. Transitional positions outline the boundary of anisotropic dendrite selection, where dendrite boundaries misalign and stray grain occur to actively serve as easy paths for crack propagation. Dendrite trunk spacing significantly varies with niobium alloying. Niobium-rich addition sensitively favors fine-scale dendrite trunk spacing, beneficially decreases the dendrite trunk gradient, and impedes the stray grain formation potential to resist interdendritic solidification cracking.

3.3 Effect of niobium alloying on non-equilibrium solidification behavior of single crystal superalloys

The effect of niobium alloying on eutectic behavior is shown in Fig. 4.

In Fig. 4a, first of all, the effect of niobium-rich addition on promoting the formation of major phases, γ/NbC and γ/Laves, is rather apparent. The minimum amount of eutectic-type constituents exists near the root of the weld pool. Secondly, the amount of the eutectic-type constituents is associated with the crack self-repairmen due to the accessibility to molten weld pool to supply feeding channel

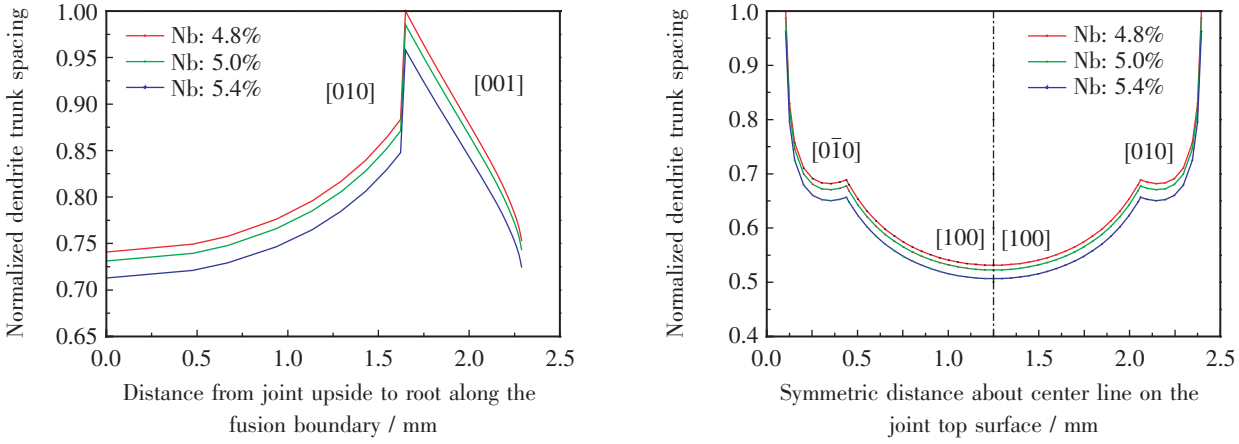

(a) Longitudinal dendrite morphology (b) Transverse dendrite morphology

Fig. 3 The role of niobium alloying in dendrite morphology

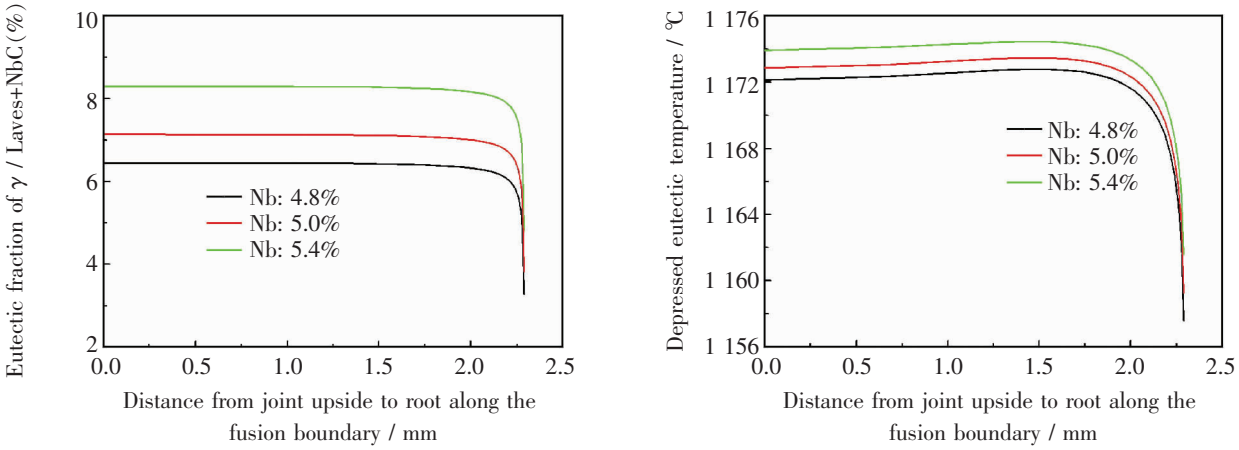

(a) Fraction of eutectics (b) Eutectic temperature

Fig. 4 The role of niobium alloying in solidification behavior along fusion boundary

of available backfill. The less addition of niobium, the less eutectic-type constituents will be produced and aid in minimizing the risk of cracking through self-healing. Finally, the backfill throughout the arterial crack network in the weld pool actively self-repairs the severe cracking, and this kind of synergistic crack self-repairmen phenomenon is also available to polycrystalline superalloys. In Fig. 4b, first of all, a small variation of niobium alloying differs the actual solidus temperature where the formation of the γ/Laves eutectic-type constituent occurs. The depressed eutectic temperature diminishes near the bottom of the weld pool and causes a steep temperature gradient. High-niobium concentration stabilizes primary solidification path of L $\rightarrow\gamma$ + Laves reaction, increases the solidification temperature of terminal stage, narrows the effective solidification temperature range, refines microstructure, decreases weld pool geometry, and thus promotes a significant improvement in cracking resistance. Secondly, it also decreases the available time and amount of terminal liquid for self-repairmen by backfill to bridge the cracking. Finally, the major impetus to repair incipient cracking by spontaneous mergence of portion of arterial crack network through backfill without adopting welding consumables leads to control niobium composition in the material and non-equilibrium solidification behavior.

3.4 Effect of grain boundary carbon alloying on development of intergranular liquid film

Metallurgically, the effect of carbon concentration at grain boundary on thermal stability of niobium carbide particle is shown in Fig. 5.

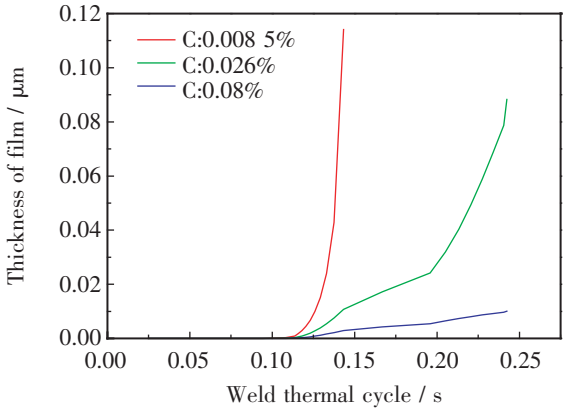

(a) Thickness of intergranular liquid film

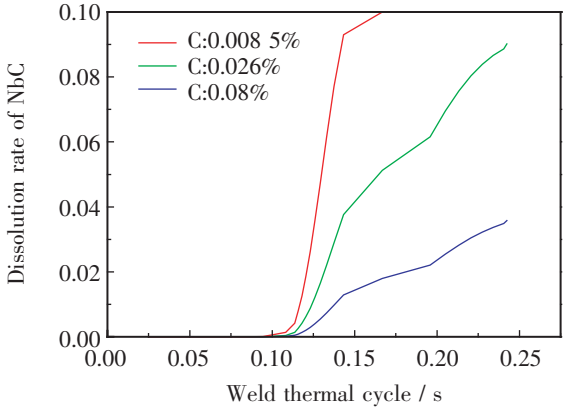

(b) Dissolution rate of NbC with carbon alloying

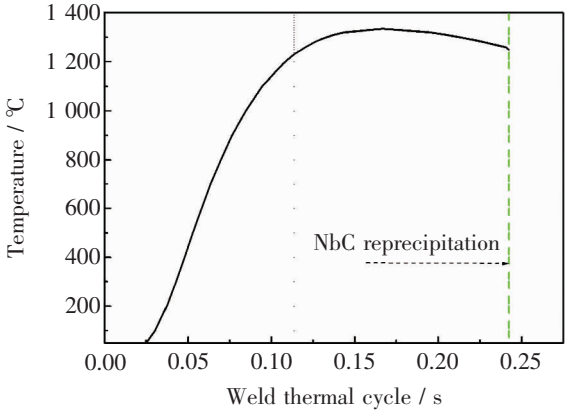

(c) Temperature distribution

Fig. 5 The effect of carbon concentration at grain boundary on thermal stability of niobium carbide particle

In Fig. 5a, carbon-rich grain boundary is stably resistant to liquation cracking in that it delays the onset of dissolution of niobium carbide particle and less contributes to the thickness of incipient intergranular liquid film. Moreover, high carbon and low niobium concentrations extensively adjust the primary solidification path towards eutectic-type reaction $L \rightarrow \gamma + NbC$ at high temperature instead of $L \rightarrow \gamma +$ Laves at the terminal stages of solidification, and thus decrease the solidification temperature range. In Fig. 5b, dissolution rate of niobium carbide particle is strongly contingent upon the thermal path and grain boundary carbon alloying. Niobium carbide particle around low-carbon grain boundary is more susceptible to dissolution and facilitates an extensive increment of the thickness of intergranular liquid film. However, the enrichment of carbon concentration at grain boundary retards the dissolution of niobium carbide particle.

The role of grain boundary carbon alloying and particle size in particle dissolution during rapid on-heating part of weld thermal cycle is shown in Fig. 6. In Fig. 6a, the niobium carbon particles completely dissolve in the molten weld pool regardless of the carbon concentration and particle size, and become small in the mushy zone and HAZ due to insufficient time and temperature. High-carbon grain boundary induces partial particle dissolution. In Fig. 6b, as the temperature further increases, submicron size particles readily dissolve in the mushy zone and HAZ and directly contribute to intergranular liquid film. Fine particle characterizes appreciable dissolution during up to the peak temperature, while coarse one is refractory. There is still large abundance of partially dissolved particles that preclude the grain growth.

3.5 Effect of heat input and niobium alloying on synergistic self-repairmen of arterial crack network

The role of welding parameters in cumulative thickness of intergranular liquid film and fraction of eutectics is shown in Fig. 7. In Fig. 7a, the major eutectic-type constituents of γ/NbC and γ/Laves enrich niobium, and heterogeneously mix inside the repaired crack network to give rise to incoherent interface and locally compromise the HAZ integrity. First of all, high heat input produces large amount of eutectic-type constituents, however, the mere

pursuit of sufficient amount of liquid to initiate the backfill through the mushy zone to heal incipient cracking by further increasing heat input is incapable of a preference because high heat input simultaneously induces other crack-susceptible consequences. Niobium-rich concentration advances eutectic-type reactions and stabilizes primary solidification path in the backfill. Secondly, the heat input should not only withstand excessive niobium segregation and optimize weld pool dynamics to expel the interdendritic liquid into crack network, but also suffice the adequate time of backfill to heal the incipient crack morphology. In Fig. 7b, first of all, high heat input produces thick intergranular liquid film as a result of dissolution of niobium carbide particles, while low heat input incurs less intergranular liquid. Secondly, continuous and thicker intergranular liquid film is more prone to engender grain boundaries detachment due to incapable accommodation of the local tensile components, and therefore is fairly susceptible to intergranular liquation cracking, while thinner one is chemically eliminated by subgrain coalescence and liquid film migration owing to release of coherency strain energy.

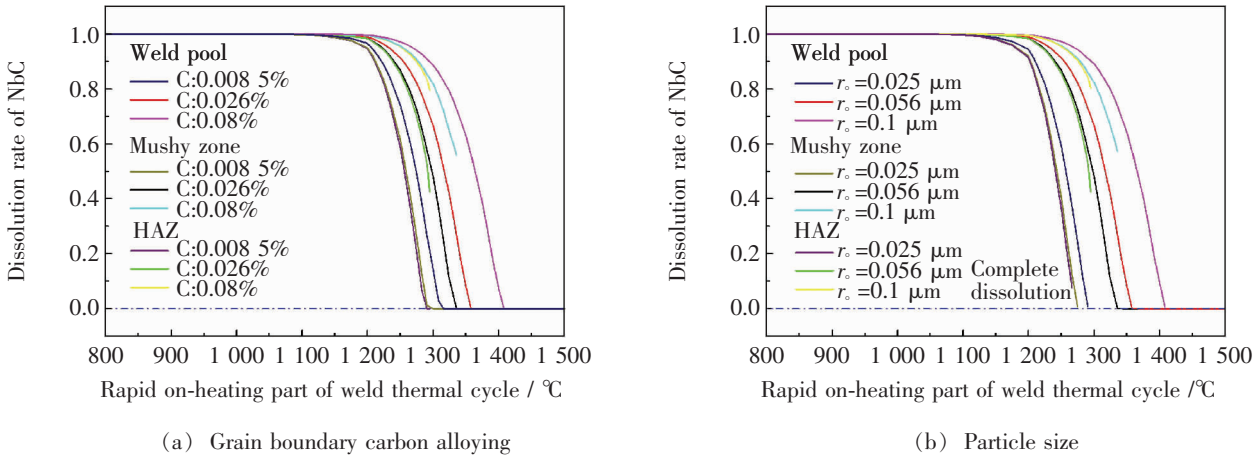

(a) Grain boundary carbon alloying (b) Particle size

Fig. 6 Dissolution of niobium carbide particle during weld thermal cycle

The role of welding parameters in the response of repaired crack network at high energy sites within recrystallized HAZ is shown in Fig. 8. In Fig. 8a, first of all, high heat input significantly widens the sensitive time duration, and induces complete particle dissolution to deteriorate grain boundary liquation, while low heat input delays grain boundary liquation. The longer the sensitive time interval of cracking, the greater is the presence of the risk of cracking. Secondly, according to[17-18], the critical range of weld thermal cycle near the solid-liquid interface of weld pool is of the typical order of 0.1 s during laser welding; therefore, the theoretical predictions by the criterion are acceptable. Finally, it is also controversial that high heat input provides longer time for backfill to self-repair arterial crack network, but this contribution is inferior to that of degradation of cracking. In Fig. 8b, internal dendrite type of substructure occurs during solidification of backfill near the fusion boundary. The size and morphology of crystallographic substructure of backfill inside narrow crack network are dependent on heat input. High heat input produces coarser substructure, while low heat input incurs finer subdendrite to facilitate microstructural control and substructural integrity. The theoretical predictions of subdendrite arm spacing of backfill are order of 0.1 – 1 micron and comparable with the experimental measurement. In Fig. 8c, microcrack lengths beneath the surface widely vary with different welding conditions, and the relationship between welding parameter and total crack length is approximately linear. The theoretical predictions of cracking susceptibility in the foregoing discussions are in satisfactory agreement with the experimental results indirectly.

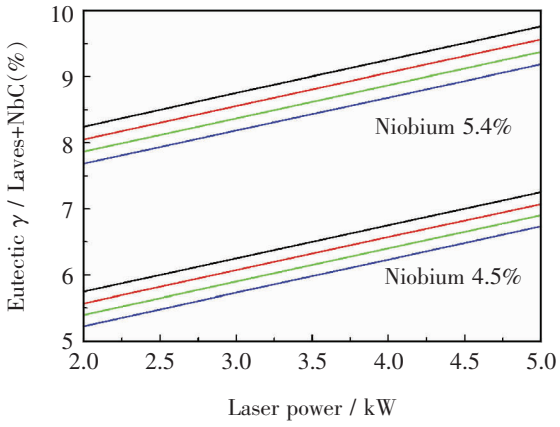

(a) Fraction of eutectics

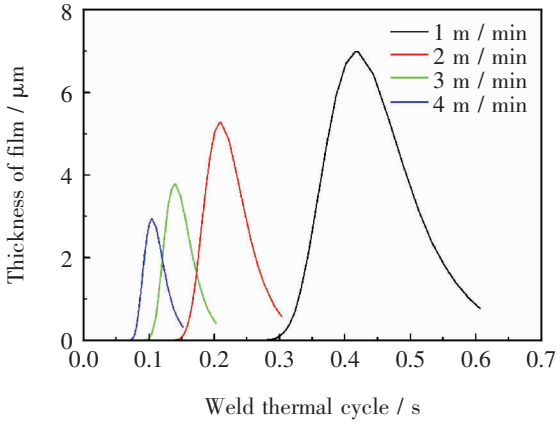

(b) Thickness of intergranular liquid film

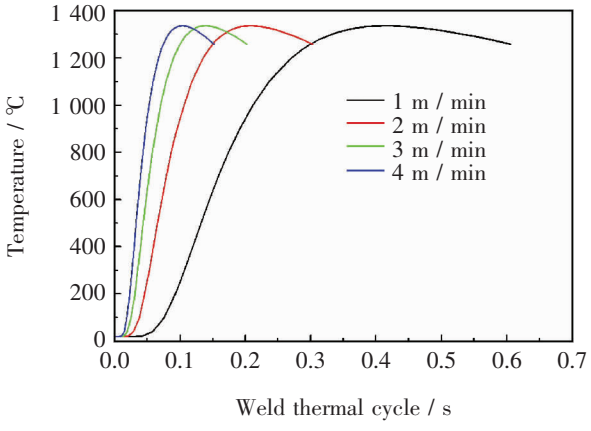

(c) Temperature distribution

Fig. 7 The role of welding parameters in crack healing characteristics surrounding crack edges

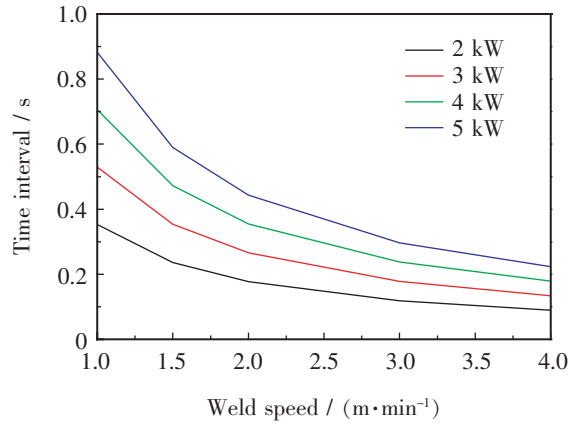

(a) Sensitive time interval of cracking

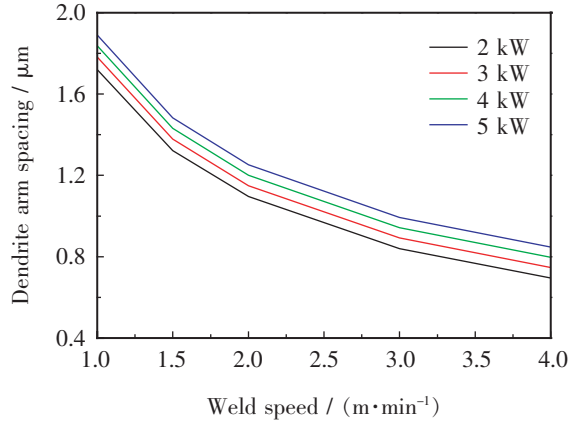

(b) Dendrite arm spacing near the backfill

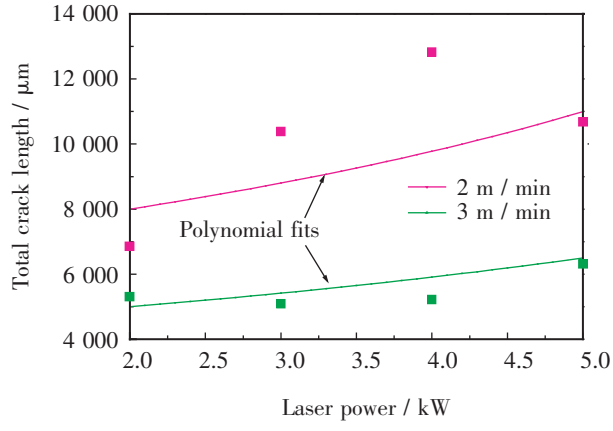

(c) Experimental results

Fig. 8 The role of welding parameters in the response of repaired crack network at high energy sites within recrystallized HAZ

4 Conclusions

(1) Niobium-rich alloying beneficially refines weld microstructure to impede the strain grain formation potential, stabilizes the primary solidification path, increases the solidification temperature of terminal stage and concomitantly decreases the weld pool geometry.

(2) Niobium carbide particle around low-carbon grain boundary is more susceptible to complete dissolution to give rise to thick intergranular liquid film, while niobium carbide particle around high-carbon grain boundary is more thermal stable to less contribute to the integranular liquid film.

(3) High heat input produces large amount of eutectics and thick intergranular liquid film. Mere increasing heat input is incapable of healing arterial crack network through backfilling, because high heat input simultaneously induces other cracking-susceptible consequences.

(4) The theoretical predictions of cracking susceptibility are indirectly verified by experimental results in a rather satisfactory manner.

References

[1] Vitek J M. The effect of welding conditions on stray grain formation in single crystal welds-theoretical analysis. Acta Materialia, 2005, 53(1): 53 – 67.

[2] Dye D, Hunziker O, Reed R C. Numerical analysis of the weldability of superalloys. Acta Materialia, 2001, 49(4): 683 – 697.

[3] Liu W P, Dupont J N. Effects of melt-pool geometry on crystal growth and microstructure development in laser surface-melted superalloy single crystals. Mathematical modeling of single-crystal growth in a melt pool (part Ⅰ). Acta Materialia, 2004, 52(16): 4833 – 4847.

[4] Trivedi R, Kurz W. Morphological stability of a planar interface under rapid solution conditions. Acta Metallurgica, 1986, 34(8): 1663 – 1670.

[5] Kurz W, Trivedi R. Eutectic growth under rapid solidification conditions. Metallurgical Transactions A, 1991, 22A(12): 3051 – 3057.

[6] Wang K, Wang H F, Liu F, et al. Modeling rapid solidification of multi-component concentrated alloys. Acta Materialia, 2013, 61(4): 1359 – 1372.

[7] Galenko P K, Reutzel S, Herlach D M, et al. Dendritic solidification in undercooled Ni-Zr-Al melts: Experiments and modeling. Acta Materialia, 2009, 57(20): 6166 – 6175.

[8] Kurz W, Giovanola B, Trived R. Theory of microstructural development during rapid solidification. Acta Metallurgica, 1986, 34(5): 823 – 830.

[9] Sarreal J A, Abbaschian G J. The effect of solidification rate on microsegregation. Metallurgical Transactions A, 1986, 17(11): 2063 – 2073.

[10] Radhakrishnan B, Thompson R G. A model for the formation and solidification of grain boundary liquid in the heat-affected zone (HAZ) of welds. Metallurgical Transactions A, 1992, 23(6): 1783 – 1798.

[11] Pottlacher G, Hosaeus H, Kaschnitz E, et al. Thermophysical properties of solid and liquid Inconel 718 Alloy. Scandinavian Journal of Metallurgy. 2002, 31(3): 161 – 168.

[12] Sawada H, Taniguchi S, Kawakami K, et al. First- principles study of interface structure and energy of Fe/NbC. Modelling and Simulation in Materials Science and Engineering, 2013, 21(4): 045012.

[13] Hunziker O, Dye D, Reed R C. On the formation of a centerline grain boundary during fusion welding. Acta Materialia, 2000, 48(17): 4191 – 4201.

[14] Damien C, Benoît To, éric A. Diffusion and segregation of niobium in fcc-nickel. Journal of Physics: Condensd Matter, 2012, 24(9): 095010.

[15] Knorovsky G A, Cieslak M J, Headley T J, et al. Inconel 718: a solidification diagram. Metallurgical Transactions A, 1989, 20(10): 2149 – 2158.

[16] Grong Øystein. Metallurgical modeling of welding (second edition). London: The Institute of Materials, 1997.

[17] Rai R, Kelly S M, Martukanitz R P, et al. A convective heat-transfer model for partial and full penetration keyhole mode laser welding of a structural steel. Metallurgical and Materials Transactions A, 2008, 39(1): 98 – 112.

[18] Lambrakos S G, Metzbower E A, Moore P G, et al. A numerical model for deep penetration welding processes. Journal of Materials Engineering and Performance, 1993, 2(6): 819 – 838.